

Online Supplementary Information

Structure of particle networks in capillary suspensions with wetting and non-wetting fluids

Frank Bossler and Erin Koos

Karlsruhe Institute of Technology, Institute for Mechanical Process Engineering and Mechanics, Straße am Forum 8, 76131 Karlsruhe, Germany

Contents

1	Preparation and properties of silica particles	1
1.1	Modified Stöber synthesis and mechanical treatment of Kromasil particles	1
1.2	Particle size distribution of Kromasil before and after dyeing	2
1.3	Contact angle variation by hydrophobization of the particle surface with TMCS	3
1.4	Determination of the refractive index of the dyed Kromasil particles	4
2	Interfacial properties of the liquid phases	5
3	Imaging of capillary suspensions	6
3.1	Computational determination of particle pair distribution functions	6
3.2	Three-dimensional images of capillary suspensions using nonporous particles	6
3.3	Pair distribution function peak shapes and locations	6
3.4	Difficulties in imaging microdroplets and microbridges	8
4	Contact angle dependent coalescence criterion for the pendular-funicular transition	10

1 Preparation and properties of silica particles

1.1 Modified Stöber synthesis and mechanical treatment of Kromasil particles

For covalently binding the fluorescent dye to the Kromasil particles, a modified Stöber synthesis was used. First, 0.012 g of the fluorescent dye rhodamine B isothiocyanate (Sigma-Aldrich, Steinheim, Germany) and 12 μL of 3-(triethoxysilyl)-propylamine (Merck, Darmstadt, Germany) were covalently bonded using 10 mL of ethanol as a solvent. This coupling reaction took place under gentle stirring for 18-24 h with a magnetic stirrer. Afterwards, the Stöber reaction was started by assembling 110 mL ethanol, 15.7 g Kromasil silica particles, 10.8 mL of 32% ammonia solution (Carl Roth, Karlsruhe, Germany),

the coupled dye solution, and 6 mL tetraethyl orthosilicate (TEOS, Merck, Darmstadt, Germany) in a closed round-bottom flask. The vessel was attached to a shaking table at a frequency of 275 rpm to provide continuous oscillation. This mixing method was chosen to avoid particle breakup, which occurred when a magnetic stirrer was used (see Fig. S1). Another 6.4 mL of TEOS and 5.4 mL of ultrapure water were added to the reaction vessel after 24 h. During the reaction, the TEOS as well as the coupled dye are covalently bonded to the silica surface. The dyed particles were separated after another 24 h by centrifugation for 5 min at 500 rpm (higher speeds also led to particle breakup), rinsed six times in ethanol to remove any remaining reactants, dried overnight at 70°C and finally kept under vacuum for 1 h to remove any remaining ethanol.

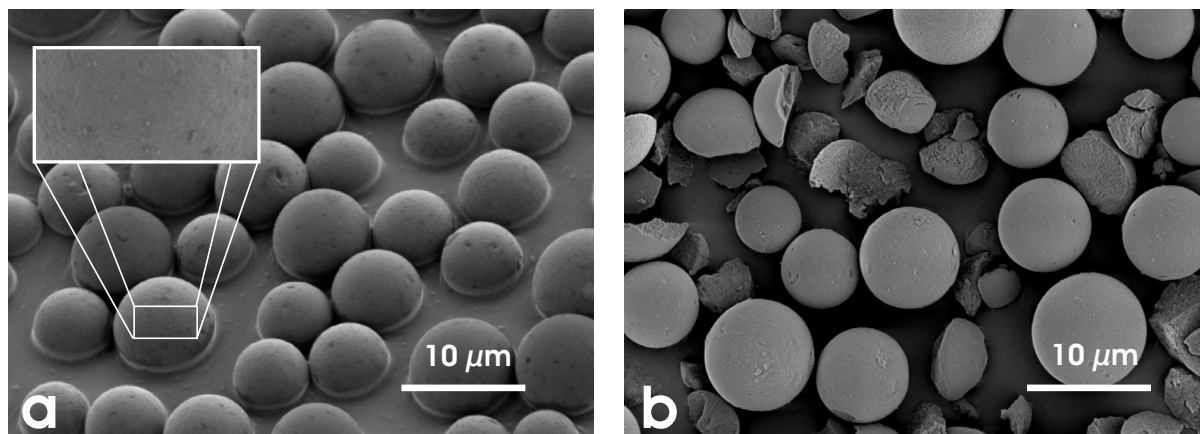


Figure S1: Scanning electron microscopy images of Kromasil particles after the dyeing reaction. (a) Spherical particles obtained after reaction as described in the main text and supplementary information. The inset gives a magnified view of the particle surface with width 5 μm . (b) Particle fracture due to magnetic stirring and high centrifugation speed (2000 rpm).

When this dyeing procedure is used, all particles retain their spherical shape (Fig. S1.a). The particles will break if the particle reaction takes place under magnetic stirring or if the centrifuge speed used in the particle washing steps is too high (Fig. S1.b). Broken particles are unusable for the preparation of capillary suspension model systems, as the sharp broken edges and the roughness of the raised inner surface complicate the contact angle determination. Furthermore, the non-spherical shape of broken particles can lead to serious errors in the MATLAB image evaluation. When the samples were mixed using an ultrasonic horn, no relevant particle breakup could be observed (approximately less than 5 broken pieces per 1000 particles). This can be directly observed from the 2D and 3D confocal images of the samples where all of the particles appear spherical (Fig. 2, 3 and 6 in the main text, Fig. S4 in the supplementary information).

1.2 Particle size distribution of Kromasil before and after dyeing

The particle size was measured both prior to and following dyeing to assess any changes from the reaction. The size distribution was determined by Fraunhofer light diffraction (Helos H0309, Sympatec, Clausthal-Zellerfeld, Germany) using an ultrasonic wet dispersing unit (Quixel, Sympatec) where the particles are dispersed in ethanol. The displayed

curves for Kromasil before and after dyeing (Fig. S2) are averaged from five measure-

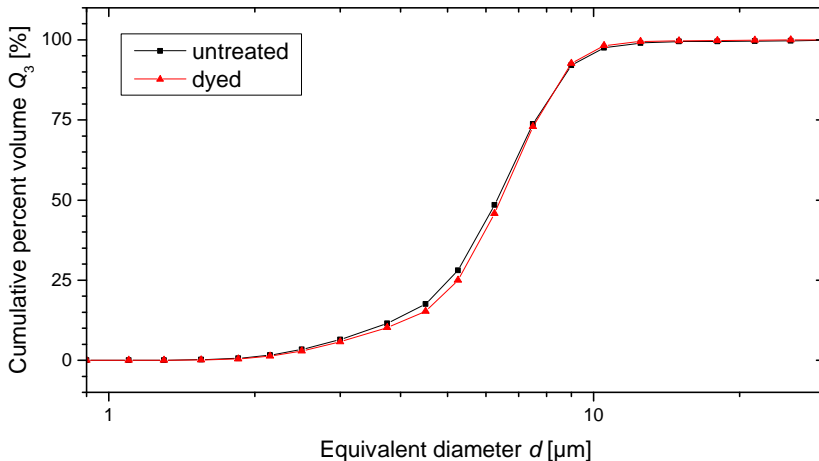


Figure S2: Particle size distribution of Kromasil particles before (black squares) and after (red triangles) the dyeing reaction.

ments. Measurement error (not shown) is about 40 nm for the characteristic diameter $d_{50,3}$. The mean particle size increases only very slightly due to the dyeing process and is in the range of the measurement error. No significant differences between the size distribution before and after dyeing are visible. Thus, particle fracturing due to stirring or centrifuging, particle merging, or the production of additional small new particles due to the Stöber reaction does not occur during the dyeing process.

1.3 Contact angle variation by hydrophobization of the particle surface with TMCS

Additional reaction steps were completed using the dyed porous silica particles to further modify the particle surface. An overview of the prepared particle types used in this study is shown in Table S1, including both porous and nonporous particles. To produce nonporous particles, the modified Stöber reaction was repeated using small amounts of dyed particles, with some differences in the reaction scheme, see Materials and Methods section in the main text.

To change the contact angle, the silica surface was treated with trimethyl chlorosilane (TMCS, Alfa Aesar, Karlsruhe, Germany). When exposed to TMCS, the $-\text{OH}$ groups on the silica surface are replaced by trimethylsilyl groups ($-\text{Si}-(\text{CH}_3)_3$) making the particle surface more hydrophobic (1). The number of replaced groups depends on the reaction time, the TMCS concentration and the reaction kinetics (2). Degassing of the silica particles before the reaction can lead to more reproducible reaction kinetics (3), therefore the dyed particles were placed under vacuum for at least 1 h before being added to the reaction vessel. Different degrees of hydrophobicity were reached by choosing different amounts of TMCS between 10 and 200 μL TMCS per gram silica as shown in Table S1. First, TMCS was distributed in cyclohexane (Merck, Darmstadt, Germany) at room temperature after which the silica particles were added. Following 3 h of constant shaking,

Table S1: Chemically modified particles prepared in this study. The reaction time was 3 hours for all TMCS reactions. The contact angle θ was measured as described in the methods and materials section of the main text.

TMCS concentration [μL per gram particles]	Contact angle, θ [$^\circ$]
nonporous particles	
10	40 ± 6
20	61 ± 4
40	94 ± 5
porous particles	
0	38 ± 4
10	67 ± 14
26	72 ± 4
23	90 ± 5
35	109 ± 5
29	115 ± 4
41	117 ± 6
47	133 ± 4
200	139 ± 10
200	147 ± 7

the reaction was interrupted by centrifuging the particles, washing them four times in cyclohexane, drying them overnight at room temperature, and then degassing them for 1 h under vacuum.

1.4 Determination of the refractive index of the dyed Kromasil particles

The particle refractive index of dyed Kromasil particles was measured using an aqueous solution of sodium iodide (NaI, AppliChem GmbH, Darmstadt, Germany). The refractive index dependence of aqueous solutions on the NaI concentration was determined beforehand by measuring a concentration series of eleven NaI solutions between 0%wt and 60%wt NaI with an Abbe refractometer, where the refractive index n was fit using the empirical relation

$$n = 1.333 + 1.340 \cdot 10^{-3}c + 1.750 \cdot 10^{-5}c^2 - 1.697 \cdot 10^{-7}c^3 + 3.189 \cdot 10^{-9}c^4 \quad (1)$$

with the NaI concentration c in %wt. Ultrapure water was added dropwise under constant stirring to a 57% NaI solution ($n = 1.469$) with added Kromasil particles until the sample looked transparent. The amount of added water was determined by measuring the total increase in sample weight. The refractive index of the particles could be deduced by calculating the actual NaI concentration and then using equation 1 to determine the refractive index.

2 Interfacial properties of the liquid phases

The bulk fluid used for preparation of capillary suspensions is a mixture of 84%vol dodecane and 16%vol 1,2-cyclohexane dicarboxylic acid diisononyl ester (Hexamoll[®] DINCH[®]). While dodecane is nonpolar, the ester is slightly polar and thus expected to be surface active against the polar secondary fluid used in the capillary suspensions (a 86%wt/14%wt glycerol/water mixture). To survey this surface activity, a pendant drop apparatus was used to measure interfacial tensions of Hexamoll/dodecane mixtures with varied volume ratio from 0 (pure dodecane) to 1 (pure Hexamoll) against pure water and against a glycerol/water mixture with 0.91/0.09 volume ratio. The slight deviation in glycerol/water ratio was necessary due to the pendant drop method requiring a mismatch in refractive index, which is obviously avoided in the actual confocal microscopy system. The results are shown in (Fig. S3). As water is more polar than glycerol, the surface

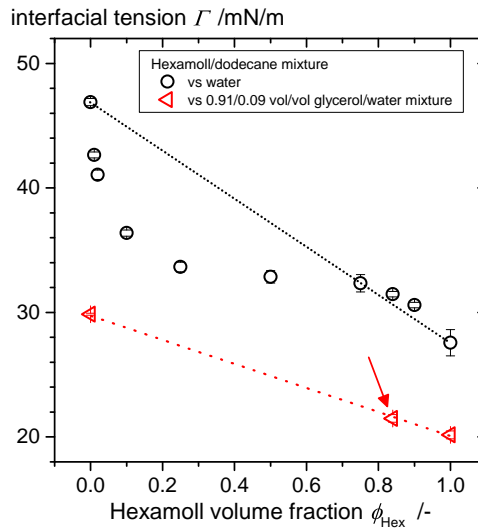


Figure S3: Interfacial tension of Hexamoll/dodecane mixtures with varied volume ratio against pure water (black circles) and against aqueous glycerol solutions (red triangles). The dashed straight lines are the ratio dependent interfacial tensions if there is no surface activity. The red arrow marks the fluid combination closest to the one used in all of the prepared capillary suspension samples.

activity of Hexamoll should be more pronounced against pure water than against glycerol/water mixtures. The dashed black line in the diagram identifies a theoretical linear dependence of the surface tension on the Hexamoll/dodecane ratio. While for low loadings of Hexamoll a strong reduction in the interfacial tension below this line is obvious, the measured values approach the linear dependence for Hexamoll loadings > 0.75 . This data proves relevant surface activity of Hexamoll against water, as expected. This surface activity is irrelevant at high Hexamoll loadings as used in all of the samples prepared in the main study. The data shown as red triangles in Fig. S3 further corroborate the lack of significant surface activity near the ratios used for confocal experiments.

3 Imaging of capillary suspensions

3.1 Computational determination of particle pair distribution functions

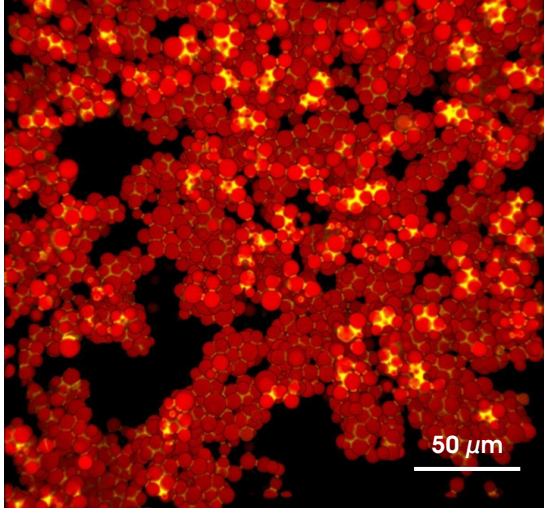
Particle localization with MATLAB was based on a modification of the 2D particle tracking algorithm of Crocker and Grier (4), which had been further developed for 3D detection by Weeks (5; 6). As the particles in this study have a broad size distribution and some confocal images were too noisy (taking the much bigger pixel number per particle into account, compared to the original Crocker and Grier study) some more elaborate processing steps were necessary. Following image smoothing with a Wiener filter, the image was convolved with a mask having the shape of a 3D Gaussian distribution. The Kilfoil groups MATLAB version (7; 8) of the Weeks algorithm was used for the convolution. To take the particle size distribution into account, five convolutions with five different mask diameters were made, overlaying the maximum values of the five different convolved images to get an optimized image – a method developed by Wenzl et al. and described in their publication in much more detail (9). From the multiply convolved image, the particle positions were detected using the original Weeks algorithm provided in the Kilfoil code. Some particles missed by the algorithm were afterwards detected manually to ensure complete data sets of spatial particle positions. Finally, the particle centers were refined. Discrete particle pair distribution functions $g(r/R)$ were computed from the particle positions using the method described by Weeks (10). Fractal dimensionalities were calculated, using the method described by Dinsmore et al. (11). The fractal dimensionality D_f is obtained by fitting a power law to the determined pair distribution function $g(r/R)$ and then using the proportionality $g(r/R) - 1 \propto (r/R)^{(D_f-3)}$.

3.2 Three-dimensional images of capillary suspensions using nonporous particles

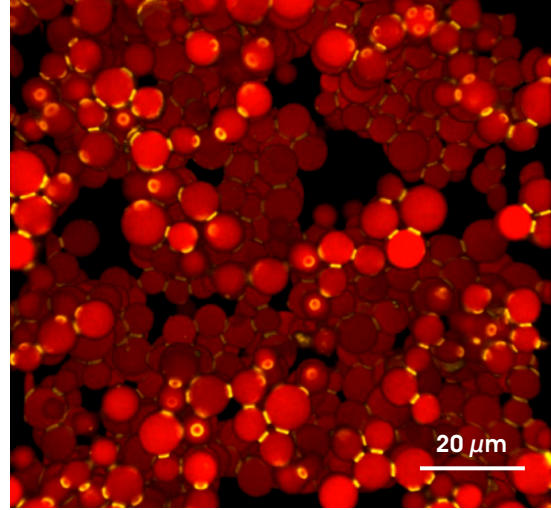
3D images of the capillary suspensions with nonporous particles have been reconstructed by overlaying all voxels of both detected channels using ImageJ. The resulting images for the funicular-like (Fig. S4.a) and the binary bridged pendular state (Fig. S4.b) as well as for the capillary state (Fig. S4.c) are given here. As additional supplementary information, videos showing the 3D images of these three samples from different angles are also provided on the Langmuir Journal web page.

3.3 Pair distribution function peak shapes and locations

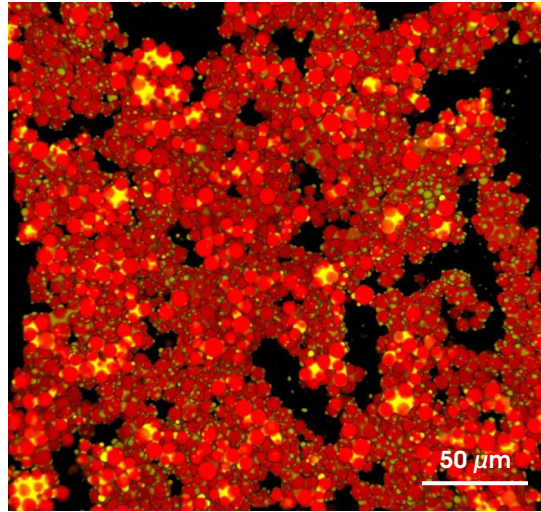
The pair distribution function (PDF) gives information on the relative particle distances and configuration. In an idealized linear chain of monodisperse particles, the pair distribution function will have a discrete value located at $2R$ denoting the separation of two particles in contact with additional contributions located at $4R$, $6R$ and so forth. In real systems, these peaks have some finite width and are shifted to smaller distance values to account for bends or branches in the chain as well as the distribution of particle sizes with clear troughs between these peaks and decaying amplitude as the correlation between particle positions far from the origin is lost.



(a) Funicular-like pendular state with three phase contact angle $\theta = 40^\circ$.



(b) Pendular state (binary bridges) with $\theta = 61^\circ$.



(c) Capillary state with $\theta = 94^\circ$.

Figure S4: Three-dimensional reconstructions of confocal images of capillary suspensions. All samples consist of nonporous particles (red, $\phi_{\text{solid}} = 0.25$) and added secondary fluid (yellow, $\phi_{\text{sec}} = 0.0225$). The reconstruction was done with ImageJ. All voxels of both detection channels have been overlaid. The image size is $246 \times 246 \times 40 \mu\text{m}$ in (a) and (c) and $102 \times 102 \times 40 \mu\text{m}$ in (b).

For the 61° sample, there are clear peaks located at $2R$ and $3.75R$ with a trough between. This trough, located at $3R$ has a value $g(3R) = 1$ indicating a clear deficit of particles at this intermediate distance. The shift can either be due to a clustering of particles (chain-blob morphology) or bended chains. There are very few close-packed clusters formed in this sample as indicated by the confocal images. Instead, we hypothesize that this shift indicates a tortuous network with an average opening angle of 140° .

However, such close-packed clusters are visible in the 94° sample. Following the method of Arkus, Manoharan and Brenner, we can derive the ground state energy clusters and their interparticle separations (12; 13). For example, a five particle triangular bipyramid ($n = 5$, D_{3h}) has a particle separation of $4\sqrt{2}/3R \approx 3.27R$ for the distance between the top and bottom particles in addition to the $2R$ distance between adjacent particles. These particle separations and the number of particle pairs at each distance is summarized in Table S2. The presence of particle clusters will contribute to the value of the PDF at values between $2R$ and $4R$. As the clusters grow in size and variety, the width of the secondary peak, which was centered at $4R$ for ideal linear particle chains, should shift to lower distances and broaden. The trough at $3R$ should also begin to disappear. This is the case with the 94° sample where the peak is centered at $\sim 3.6R$ and the difference between the peak and trough values is very small. This is consistent with the previous computational model, which predicted close-packed tetrahedral clusters with no preferred configuration at low contact angles in the capillary state (14).

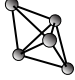
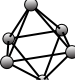
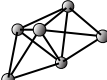

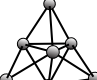

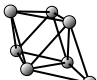

In the funicular-like 40° sample, close-packed clusters are visible in the confocal images, but the PDF shows a clear trough at $3R$ and the peak is centered at the relatively large value of $4R$. This secondary peak is wider than in the binary bridge sample (61°) with a shoulder at higher separations. Given the almost nonexistent contribution in the PDF at $3R$, we can conclude that while such particle clusters exist in this funicular-like sample, they are unlikely to be close-packed or are more likely to be non-rigid. This sample should also exhibit a decreased variety of the clusters with more linear, low symmetry configurations preferred over the compact, high symmetry clusters leading to the shoulder at higher particle separations. This would correspond to an entropic attachment of new particles to an existing cluster as was found for “sticky” particles (15). We should note, however, that the aggregates of bridged dimers or trimers have preferred binding sites, dependent on the partial coverage with second fluid, such that they cannot be directly compared to clusters formed from particles with a depletion interaction or even to individual particle aggregation where the entire particle surface is covered in a thin layer of secondary fluid.

3.4 Difficulties in imaging microdroplets and microbridges

As discussed in section 3.3 of the main text, microbridges should be present in the samples made with porous particles where the contact angle is slightly below 90° . These microbridges and microdroplets are very difficult to detect due to the broad size distribution of secondary fluid droplets. The larger droplets are detected correctly if the laser intensity or detector gain of the confocal microscope is relatively low, but the smallest droplets are invisible due to their low absolute dye content (Fig. S5.a). If the laser intensity or detector gain is increased, the small droplets can become visible – see the tiny bridges in Fig. S5.b – but the large droplets saturate neighboring voxels in the image. The contour

of these larger droplets then cannot be detected correctly. Figure S5 shows an exemplary 2D image of the detected secondary phase channel. The sample shown consists of porous particles ($\phi_{\text{solid}} = 0.25$) with a secondary phase content of $\phi_{\text{sec}} = 0.0225$ and a contact angle of $\theta \approx 115^\circ$. Insufficient mixing conditions have been chosen here for sample preparation as the difficulties in imaging these microbridges become obvious. First, the secondary phase and bulk fluid were emulsified by ultrasound. Then, the particles were stirred into the non-stabilized emulsion with a magnetic stirrer, a process that does not lead to the formation of a stable homogeneous capillary suspension. The first image (Fig. S5.a) was taken while applying a laser intensity of 0.2 W, an intensity that was also used for all of the figures shown in the main text. None of the small bridges between the

Table S2: Interparticle separations and number of pairs for close-packed clusters with 5, 6 and 7 particles.

Configuration	Particle separations (number of pairs \times distance)			
5 particles				
D_{3h} 	$9 \times 2R,$	$1 \times 4\sqrt{\frac{2}{3}}R$		
6 particles				
O_h 	$12 \times 2R,$	$3 \times 2\sqrt{2}R$		
C_{2v} 	$12 \times 2R,$	$2 \times 4\sqrt{\frac{2}{3}}R,$	$1 \times \frac{10}{3}R$	
7 particles				
C_{2v} 	$15 \times 2R,$	$3 \times 4\sqrt{\frac{2}{3}}R,$	$2 \times \frac{10}{3}R,$	$1 \times \frac{8}{9}\sqrt{6}R$
C_{3v} 	$15 \times 2R,$	$3 \times 4\sqrt{\frac{2}{3}}R,$	$3 \times \frac{10}{3}R$	
C_2 	$15 \times 2R,$	$3 \times 4\sqrt{\frac{2}{3}}R,$	$2 \times \frac{10}{3}R,$	$1 \times \frac{2}{3}\sqrt{\frac{107}{3}}R$
C_{3v} 	$15 \times 2R,$	$3 \times 2\sqrt{2}R,$	$3 \times 2\sqrt{3}R$	
D_{5h} 	$15 \times 2R,$	$5 \times \sqrt{2(3 + \sqrt{5})}R,$	$1 \times 2\sqrt{2 - \frac{2}{\sqrt{5}}}R$	

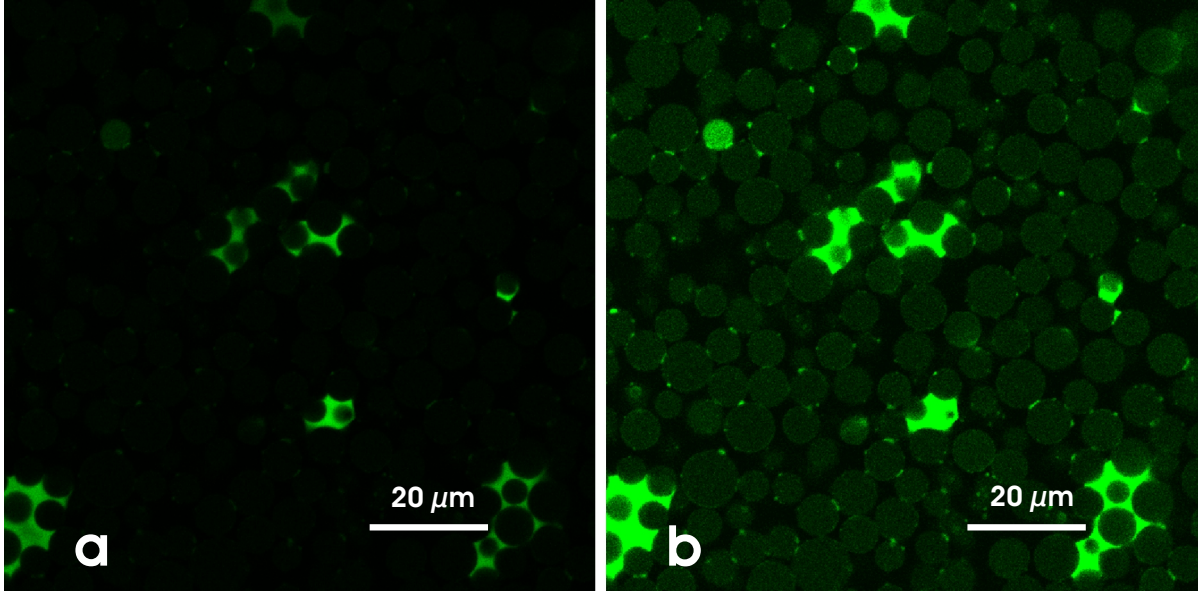


Figure S5: Effect of the laser intensity on the detected secondary phase signal for a sample with porous particles ($\phi_{\text{solid}} = 0.25$, $\phi_{\text{sec}} = 0.03$, $\theta \approx 115^\circ$). Insufficient mixing conditions were used for sample preparation and a stable capillary suspension does not form. The images show a 2D image of the secondary phase, excited by the 488 nm laser. (a) 0.2 W laser intensity where separate sharp-edged droplets of secondary phase are visible. (b) 1.2 W laser intensity. Tiny microbridges are visible, which cannot be seen in the 0.2 W image, but the large droplets outshine the image and their contour becomes poorly defined. Crosstalk from the Rhodamin B dye also begins to materialize.

particles are visible here, only some separate large droplets. The small bridges become visible when the intensity is increased to 1.2 W. Such images, however, are problematic for computational analysis due to the oversaturation present particularly for particles surrounded by droplets. Additionally there is a signal detected inside of the particles. While this could be due to very small secondary phase droplets inside of the particles, this effect can more likely be assigned to crosstalk from the Rhodamine B dye as the contact angle is greater than 90° and crosstalk was also observed when the laser intensity was increased for suspensions without any secondary fluid.

4 Contact angle dependent coalescence criterion for the pendular-funicular transition

As described in the main text (section 3.1), the samples with preferentially wetting secondary liquid can undergo a transition from the pendular state with a majority of binary bridges to a funicular-like state with coalesced bridges. The criterion used in the main text for calculating the transition volume can be explained using the geometrical scheme depicted in Fig. S6. If three spherical particles of equal size are in direct contact, the angle between two particle contact points is 60° . When there are capillary bridges at adjacent contact points (assuming both bridges have the same volume and shape), the

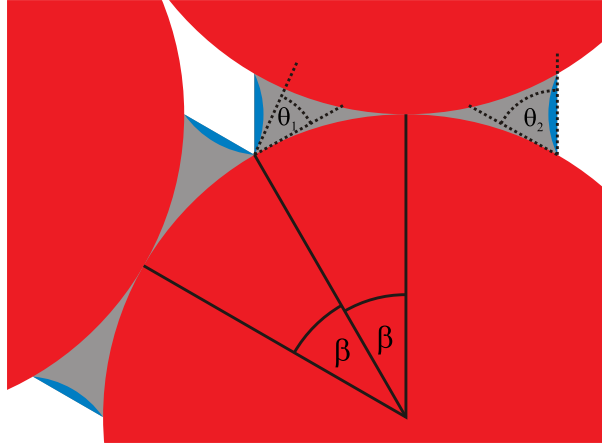


Figure S6: Schematic drawing of the contact angle dependent bridge volume. Three spherical particles (red) are in direct contact. The particles are connected by two identical binary bridges with half filling angles β . The bridge with contact angle θ_1 (gray) has a smaller volume compared to the bridge with contact angle θ_2 (gray + blue), while $\theta_2 > \theta_1$.

base of each bridge can extend up to a half filling angle $\beta < 60^\circ/2 = 30^\circ$. As soon as this critical β value is exceeded (e.g. by increasing the fluid volume per bridge), the neighboring bridges will touch and coalesce leading to a pendular-funicular transition. The gray bridge in Fig. S6 has a half filling angle $\beta = 30^\circ$ and a contact angle of $\theta_1 \approx 40^\circ$. Additional fluid volume (depicted in blue) is required to maintain $\beta = 30^\circ$ when the contact angle is increased to $\theta_2 \approx 60^\circ$. Without this volume increase, a bridge with $\theta_2 \approx 60^\circ$ would have a smaller half filling angle $\beta < 30^\circ$ and thus would not transition to the funicular state. This simple geometrical argument can easily explain why it is possible that the sample system described in the main text shows binary bridges for a contact angle of 61° while it shows the funicular-like clustered structure for a lower contact angle of 40° even though the amount of secondary fluid is the same in both samples.

References

- [1] Fuji, M, Fujimori, H, Takei, T, Watanabe, T, & Chikazawa, M. (1998) Wettability of glass-bead surface modified by trimethylchlorosilane. *The Journal of Physical Chemistry B* **102**, 10498–10504.
- [2] Suratwala, T, Hanna, M, Miller, E, Whitman, P, Thomas, I, Ehrmann, P, Maxwell, R, & Burnham, A. (2003) Surface chemistry and trimethylsilyl functionalization of Stöber silica sols. *Journal of Non-Crystalline Solids* **316**, 349–363.
- [3] Brandriss, S & Margel, S. (1993) Synthesis and characterization of self-assembled hydrophobic monolayer coatings on silica colloids. *Langmuir* **9**, 1232–1240.
- [4] Crocker, J. C & Grier, D. G. (1996) Methods of digital video microscopy for colloidal studies. *Journal of Colloid and Interface Science* **179**, 298–310.

- [5] Crocker, J. C & Weeks, E. R. Particle tracking using IDL. Retrieved from <http://www.physics.emory.edu/faculty/weeks/idl/>.
- [6] Weeks, E. R, Crocker, J. C, Levitt, A. C, Schofield, A, & Weitz, D. A. (2000) Three-dimensional direct imaging of structural relaxation near the colloidal glass transition. *Science* **287**, 627–631.
- [7] Gao, Y & Kilfoil, M. MATLAB 3D feature finding algorithms. Retrieved from <http://people.umass.edu/kilfoil/downloads.html>.
- [8] Gao, Y & Kilfoil, M. L. (2009) Accurate detection and complete tracking of large populations of features in three dimensions. *Optics Express* **17**, 4685–4704.
- [9] Wenzl, J, Seto, R, Roth, M, Butt, H.-J, & Auernhammer, G. K. (2012) Measurement of rotation of individual spherical particles in cohesive granulates. *Granular Matter* **15**, 391–400.
- [10] Weeks, E. R. How to calculate the pair correlation function $g(r)$. Retrieved from <http://www.physics.emory.edu/faculty/weeks/idl/gofr2.html>.
- [11] Dinsmore, A. D, Weeks, E. R, Prasad, V, Levitt, A. C, & Weitz, D. A. (2001) Three-dimensional confocal microscopy of colloids. *Applied Optics* **40**, 4152–4159.
- [12] Arkus, N, Manoharan, V. N, & Brenner, M. P. (2009) Minimal energy clusters of hard spheres with short range attractions. *Physical review letters* **103**, 118303.
- [13] Arkus, N, Manoharan, V. N, & Brenner, M. P. (2011) Deriving finite sphere packings. *SIAM Journal on Discrete Mathematics* **25**, 1860–1901.
- [14] Koos, E & Willenbacher, N. (2012) Particle configurations and gelation in capillary suspensions. *Soft Matter* **8**, 3988–3994.
- [15] Meng, G, Arkus, N, Brenner, M. P, & Manoharan, V. N. (2010) The free-energy landscape of clusters of attractive hard spheres. *Science* **327**, 560–563.